Underground test of gravity-related wave function collapse

Sandro Donadi,[1,†] Kristian Piscicchia,[2,3,⋆] Catalina Curceanu,[3,2]

Lajos Diósi,[4] Matthias Laubenstein,[5] Angelo Bassi,[6,7,*]

[1]*Frankfurt Institute for Advanced Studies (FIAS), Ruth-Moufang-Straße 1, 60438 Frankfurt am Main, Germany.*

[2]*Centro Fermi - Museo Storico della Fisica e Centro Studi e Ricerche "Enrico Fermi", Piazza del Viminale 1, 00184 Rome, Italy.*

[3]*INFN, Laboratori Nazionali di Frascati, Via Enrico Fermi 40, 00044 Frascati, Italy.*

[4]*Wigner Research Centre for Physics, H-1525 Budapest 114 , P.O.Box 49, Hungary.*

[5]*INFN, Laboratori Nazionali del Gran Sasso, Via G. Acitelli 22, 67100 Assergi, Italy.*

[6]*Department of Physics, University of Trieste, Strada Costiera 11, 34151 Trieste, Italy.*

[7]*INFN, Sezione di Trieste, Via Valerio 2, 34127 Trieste, Italy.*

Email: [†]*donadi@fias.uni-frankfurt.de,* [⋆]*kristian.piscicchia@cref.it,* [*]*abassi@units.it*

Roger Penrose proposed that a spatial quantum superposition collapses as a back-reaction from spacetime, which is curved in different ways by each branch of the superposition. In this sense, one speaks of gravity-related wave function collapse. He also provided a heuristic formula to compute the decay time of the superposition — similar to that suggested earlier by Lajos Diósi, hence the name Diósi-Penrose model. The collapse depends on the effective size of the mass density of particles in the superposition, and is random: this randomness shows

up as a diffusion of the particles' motion, resulting, if charged, in the emission of radiation. Here, we compute the radiation emission rate, which is faint but detectable. We then report the results of a dedicated experiment at the Gran Sasso underground laboratory to measure this radiation emission rate. Our result sets a lower bound on the effective size of the mass density of nuclei, which is about three orders of magnitude larger than previous bounds. This rules out the natural parameter-free version of the Diósi-Penrose model.

Quantum Mechanics beautifully accounts for the behaviour of microscopic systems while, in an equally beautiful but radically different way, Classical Mechanics accounts for the behaviour of macroscopic objects. The reason why the quantum properties of microscopic systems—most notably, the possibility of being in the superposition of different states at once—do not seem to carry over to larger objects, has been the subject of a debate which is as old as the quantum theory itself, as exemplified by Schrödinger's cat paradox [1].

It has been conjectured that the superposition principle, the building block of quantum theory, progressively breaks down when atoms glue together to form larger systems [2–7]. The reason is that the postulate of wave function collapse introduced by von Neumann, and now part of the standard mathematical formulation of the theory, according to which the quantum state of a system suddenly collapses at the end of a measurement process, though being very effective in describing what happens in measurements, clearly has a phenomenological flavour. There is no reason to believe that measurements are so special to temporarily suspend the quantum dynamics given by the Schrödinger equation and replace it with a completely different one. More realistically, if

collapses occur at all, they are part of the dynamics: in some cases, they are weak and can be neglected; in some other cases, such as in measurements, they become strong and rapidly change the state of a system. Decades of research in this direction has produced well-defined models accounting for the collapse of the wave function and the breakdown of the quantum superposition principle for larger systems [5,8–10], and now the rapid technological development has opened the possibility of testing them [11]. One question is left open: what triggers the collapse of the wave function?

In his lectures on gravitation, Feynman discusses how a breakdown of the quantum superposition principle at a macroscopic scale leaves open the possibility that gravity might not be quantized [12]. Along this line of thinking, Penrose (and Diósi, independently) suggested that gravity, whose effects are negligible at the level of atoms and molecules, but increase significantly at the level of macroscopic objects, could be the source of the wave function collapse: "*My own point of view is that as soon as a 'significant' amount of space-time curvature is introduced, the rules of quantum linear superposition must fail*" [13]. When a system is in a spatial quantum superposition, a corresponding superposition of two different space-times is generated. Penrose then gives arguments [14–16] as to why nature "dislikes" and, therefore, suppresses superpositions of different space-times; the more massive the system in the superposition, the larger the difference in the two space-times and the faster the wave-function collapse.

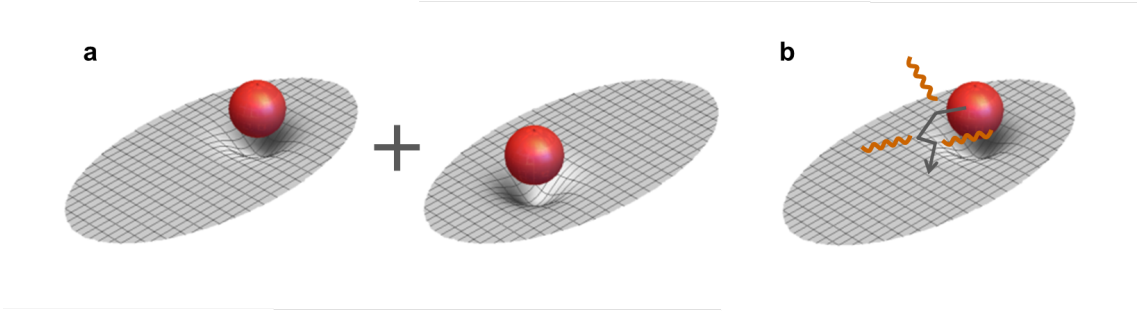

Figure 1: **The Diósi-Penrose (DP) model of gravity-related wave function collapse. a.** According to quantum gravity, a spatial quantum superposition of a system generates a superposition of different space-time curvatures, corresponding to the possible different locations of the system. Penrose argues that a superposition of different space-times is unstable and decays in time, making also the system's wave function collapse. He provides an estimate for the time of collapse as given in Eq. (1), which is the faster the larger the system, similar to that suggested earlier by Diósi. **b.** The master equation of the DP model (Eq. (3)) predicts not only the collapse of the wave function, but also an omnipresent Brownian-like diffusion for each constituent of the system. When the constituents are charged (protons and electrons), the diffusion comes with the emission of radiation, with a spectrum that depends on the configuration of the system. This is given by Eq. (4) in the range $\Delta E = (10 \div 10^5)$keV of photon energies. The predicted radiation emission is faint but potentially detectable by an experiment performed in a very low-noise environment. We performed such an experiment to rule out the original parameter-free version of the DP model.

Even without proposing a detailed mathematical model, Penrose provides a formula which estimates, in non-relativistic and weak gravitational field limits, the expected time τ_{DP} of the collapse of a quantum superposition [14]:

$$\tau_{\text{DP}} = \frac{\hbar}{\Delta E_{\text{DP}}}, \tag{1}$$

where ΔE_{DP} measures how large, in gravitational terms, the superposition is. Given a system with mass density $\mu(\boldsymbol{r})$, in the simple case of the center-of-mass being in a superposition of two states displaced by a distance $\boldsymbol{d}$:

$$\Delta E_{\text{DP}}(\boldsymbol{d}) = -8\pi G \int d\boldsymbol{r} \int d\boldsymbol{r}' \frac{\mu(\boldsymbol{r})\left[\mu(\boldsymbol{r}'+\boldsymbol{d}) - \mu(\boldsymbol{r}')\right]}{|\boldsymbol{r}-\boldsymbol{r}'|}. \tag{2}$$

Eqs. (1) and (2), which are valid in the Newtonian limit, were previously proposed by Diósi [17,18], following a different approach. For a point-like mass density $\mu(\boldsymbol{r}) = m\delta(\boldsymbol{r}-\boldsymbol{r}_0)$, Eq. (2) diverges because of the $1/r$ factor, leading to an instantaneous collapse, which is clearly wrong. To avoid this problem, one has to smear the mass density. This is implemented in different ways by Diósi and Penrose. Diósi suggests to introduce a new phenomenological parameter, measuring the spatial resolution of the mass density [19,20]; Penrose instead suggests that the mass density of a particle is given by $\mu(\boldsymbol{r}) = m|\psi(\boldsymbol{r},t)|^2$ [15], where $\psi(\boldsymbol{r},t)$ is a stationary solution of the Schrödinger-Newton equation [21,22]. For either choice, we will call R_0 the size of the particle's mass density.

A direct test of Eq. (1) requires creating a large superposition of a massive system, to guarantee that τ_{DP} is short enough for the collapse to become effective before any kind of external noise disrupts the measurement (see [23] for an alternative approach). One of the first proposals in this direction was put forward by Penrose himself and collaborators [24], who suggested a setup for

creating a spatial superposition of a mirror of mass $\sim 10^{-12}$ Kg that, according to Eq. (2), has a decay time of order $\tau_{\text{DP}} \simeq 0.002 \div 0.013$ s (see Supplementary Information), which is competitive with standard decoherence times. The major difficulty in implementing this and similar proposals consists in creating a superposition of a relatively large mass and keep it stable for times comparable to τ_{DP}. To give some examples, the largest spatial superposition so far achieved [25] is of about 0.5 m, but the systems involved are Rb atoms (mass = 1.42×10^{-25} Kg), which are too light. In matter-wave interferometry with macromolecules [26], states are delocalized over distances of hundreds nm, and masses beyond 25 kDa ($\sim 10^{-23}$ Kg), still not enough. By manipulating phononic states [27], collective superpositions of estimated 10^{16} carbon atoms (mass $\sim 10^{-10}$ Kg) are created over distances of 10^{-11} m, but the life-time of phonons is of order $\sim 10^{-12}$ s, which is too short. These numbers show that keeping the superposition time, distance and mass large enough poses still huge technological challenges. Research towards creating larger and larger superpositions is very active [28–34], but further development is needed to reach the required sensitivity.

Here we show how to test gravitational-related collapse in an indirect way, by exploiting an unavoidable side effect of the collapse: a Brownian-like diffusion of the system in space. The reason is the following. Although Penrose restrains from proposing any detailed dynamics for the collapse, as suggested in [14,15] and used explicitly in [16], the simplest assumption is that the collapse is Poissonian, as for particle decay. This minimal requirement, together with the collapse time given in Eqs. (1) and (2), implies the following Lindblad dynamics for the statistical operator $\rho(t)$ describing the state of the system (see Supplementary Information):

$$\frac{d\rho(t)}{dt} = -\frac{i}{\hbar}\left[H, \rho(t)\right] - \frac{4\pi G}{\hbar}\int d\boldsymbol{x}\int d\boldsymbol{y}\frac{1}{|\boldsymbol{x}-\boldsymbol{y}|}\left[\hat{M}(\boldsymbol{y}), \left[\hat{M}(\boldsymbol{x}), \rho(t)\right]\right]. \tag{3}$$

which is equivalent to the master equation derived in [17,18]. The first term describes the standard quantum evolution while the second term accounts for the gravity-related collapse. In Eq. (3) H is the system's Hamiltonian and $\hat{M}(\boldsymbol{x}) = \sum_n \mu_n(\boldsymbol{x}, \hat{\boldsymbol{x}}_n)$ gives the total mass density, with $\mu_n(\boldsymbol{x}, \hat{\boldsymbol{x}}_n)$ the mass density of the n-th particle, centered around $\hat{\boldsymbol{x}}_n$. Taking for example a free particle with momentum operator $\hat{\boldsymbol{p}}$, the contribution of the second term to the average momentum $\langle \boldsymbol{p} \rangle \equiv \mathrm{Tr}[\hat{\boldsymbol{p}}\rho]$ is zero, while the contribution to the average square momentum $\langle \boldsymbol{p}^2 \rangle$ increases in time. This is diffusion.

This diffusion causes a progressive heating of the system [19], specifically a steady temperature increase. Assuming a mass distribution of the nuclei with an effective size $R_0 \sim 10^{-15}$ m, the heating rate for a gas of non-interacting particles amounts to: $dT(t)/dt = 4\sqrt{\pi} m_0 G\hbar / 3k_{\mathrm{B}} R_0^3 \sim 10^{-4}$ K/s (k_{B} is Boltzmann's constant and m_0 the nucleon mass), which is in contradiction with experimental evidence [35]. The value $R_0 \sim 10^{-14}$ m is also excluded by gravitational wave detection experiments [36]. However, both results do not include the possibility of dissipative effects, which are always associated to fluctuations, which may lead to equilibrium instead of a steady growth in temperature.

Whether at thermal equilibrium or not, particles will keep fluctuating under the collapse dynamics. Since matter is made of charged particles, this process makes them constantly radiate. Therefore, a detection of the collapse-induced radiation emission is a more robust test of the model (cf. [37]) , even in presence of dissipative effects.

Starting from Eq. (3), we computed the radiation emission rate, i.e. the number of photons

emitted per unit time and unit frequency, integrated over all directions, in the range $\lambda \in (10^{-5} \div 10^{-1})$ nm, corresponding to energies $E \in (10 \div 10^{5})$ keV. The reason for choosing this range can be understood in terms of a semi-classical picture: each time a collapse occurs, particles are slightly and randomly moved. This random motion makes them emit radiation, if charged. When their separation is smaller than λ, they emit as a single object with charge equal to the total charge, which can be zero for opposite charges as for an atom. Opposite to this, when their separation is larger than λ, they emit independently. Therefore, in order to maximize the emission rate, electrons and nuclei should be independent ($\lambda <$ atomic radius), while protons in the same nucleus should behave coherently ($\lambda >$ nuclear radius). This is achieved by considering the emission of photons with wavelength in the range mentioned above. In this range, the coherent emission of protons contributes with a term proportional to $(Ne)^2$ (N is the atomic number), while electrons contribute incoherently with a weaker term proportional to Ne^2. For this reason, and also because in the range of energies considered in our experiment the electrons are relativistic, while our derivation is not, to be conservative we will neglect the contribution of the electrons in the emission rate.

The photon emission rate is discussed in the Section Methods and derived in the Supplementary Information. The calculation is lengthy. In a nutshell, starting from Eq. (3), we compute the expectation value of the photon number operator at time t, i.e. $\langle a^{\dagger}_{\mathbf{k}\mu} a_{\mathbf{k}\mu} \rangle_t$, to the first perturbative order. By taking the time derivative, summing over the photon's polarizations μ and integrating over all the directions of the emitted photon, we eventually obtain:

$$\frac{d\Gamma_t}{d\omega} = \frac{2}{3} \frac{G e^2 N^2 N_a}{\pi^{3/2} \varepsilon_0 c^3 R_0^3 \omega}, \tag{4}$$

where G, e, ε_0 and c are constants of nature with the usual meaning and N_a is the total number

of atoms. We leave R_0 as a free parameter to be bounded by experiments. Clearly, the number of emitted photons increases with the size (N_a) of the system, as there are more protons affected by the noise. The factor N^2 accounts for the quadratic dependence on the atomic number, which significantly increases the predicted effect.

We performed, for the first time, a dedicated experiment to test this model of gravity-related collapse by measuring the spontaneous radiation emission rate from a Germanium crystal and the surrounding materials in the experimental apparatus. The strong point of the experiment is that there was no need to create a spatial superposition, since according to Eq. (3) the collapse induced diffusion and the associated photons emission occur for any state, also for localized states of the system. The experiment was carried out in the low background environment of the Gran Sasso underground National Laboratory (LNGS) of INFN. The Gran Sasso Laboratory is particularly suitable for high sensitivity measurements of extremely low rate physical processes, since it is characterized by a rock overburden corresponding to a minimum thickness of 3100 m w.e. (meters of water equivalent). The environmental emissions are generated by the rock radioactivity and the residual cosmic muon flux. Given that the cosmic radiation flux is reduced by almost six orders of magnitude, the main background source in the LNGS consists of γ radiation produced by long lived γ emitting primordial isotopes and their decay products. They are part of the rocks of the Gran Sasso mountains and the concrete used to stabilize the cavity.

The setup consisted of a coaxial p-type High Purity Germanium (HPGe) detector surrounded by a complex shielding structure with the outer part made of pure lead and the inner part made of

electrolytic copper. The Germanium crystal is characterized by a diameter of 8.0 cm and a length of 8.0 cm, with an inactive layer of lithium-doped germanium of 0.075 mm all around the crystal. The active germanium volume of the detector is 375 cm^3. The outer part of the passive shielding of the HPGe detector consists of lead (30 cm from the bottom and 25 cm from the sides). The inner layer of the shielding (5 cm) is composed of electrolytic copper. The sample chamber has a volume of about 15 l ($(250 \times 250 \times 240)$ mm^3). The shield together with the cryostat are enclosed in an air tight steel housing of 1 mm thickness, which is continuously flushed with boil-off nitrogen from a liquid nitrogen storage tank, in order to reduce the contact with external air (and thus radon) to a minimum. The experimental setup is schematically shown in Fig. 2 (see also [38,39]). The data acquisition system is a Lynx Digital Signal Analyzer controlled via personal computer software GENIE 2000, both from Canberra-Mirion. In this measurement, the sample placed around the detector was 62 kg of electropolished oxygen free high conductivity copper in Marinelli geometry.

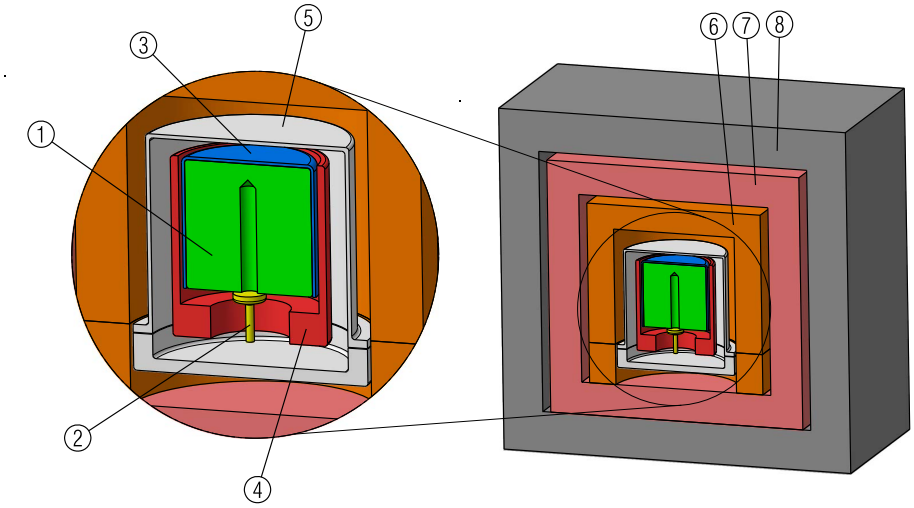

Figure 2: **Schematic representation of the experimental setup.** The experimental apparatus is based on a coaxial p-type high purity germanium detector, with the dimensions of 8.0 cm diameter and 8.0 cm length, the active volume is 375 cm^3. The detector is shielded by layers of electrolitic copper and pure lead. The inner part of the apparatus consists of the following main elements: 1 - Ge crystal, 2 - Electric contact, 3 - Plastic insulator, 4 - Copper cup, 5 - Copper end-cup, 6 - Copper block and plate, 7 - Inner Copper shield, 8 - Lead shield. In order to minimize the radon contamination an air tight steel casing (not shown) encloses the shield and is continuously flushed with boil-off nitrogen from a liquid nitrogen storage tank.

The measured emission spectrum, corresponding to a data taking period of about 62 days (August 2014 and August 2015), is shown in Fig. 3, where emission lines generated by residual radionuclides present in the setup materials are also visible. In particular, the region of the ^{60}Co lines (corresponding to the shadowed green area highlighted in the total plot) is enlarged in the inset.

Data analysis was carried out to extract the probability distribution function (pdf) of the R_0 parameter of the model. The novelty, with respect to previous investigations [40,41], is not only the dedicated experiment but also an accurate Monte Carlo (MC) characterisation, with a validated MC code based on the GEANT4 software library, of the experimental setup, which allowed to compute the background originated from known sources, determining the contribution of each component of the setup; the background simulation is described in greater detail in the Section Methods. The residual spectrum was then compared with the theoretical prediction for the collapse-induced radiation, to extract a bound on R_0.

The experimental and the MC simulated spectra agree to 88% in the energy range $\Delta E = (1000 \div 3800)$ keV, whereas in the low energy region there are larger deviations. This is mostly due to the impossibility to perfectly account for the residual cosmic rays and the bremsstrahlung caused by ^{210}Pb and its daughters in the massive lead shield. The energy range falls within the interval previously discussed for the validity of the theoretical model. Therefore we take ΔE as the energy Region Of Interest (ROI) for the following statistical analysis, the ROI is represented by the grey area in Fig. 3. In Fig. 4 the measured spectrum is compared, in the ROI, with the

simulated background distribution. The total number of simulated background counts within ΔE is $z_b = 506$ events, to be compared with the measured number $z_c = 576$ events. The reason for this low rate consists in the fact that the detector setup is especially designed for ultra low background measurements. The spectrum in Fig. 3 only contains "real" events as the digital DAQ system has a filter rejecting noise events, by their pulse shape, with efficiency better then 99%.

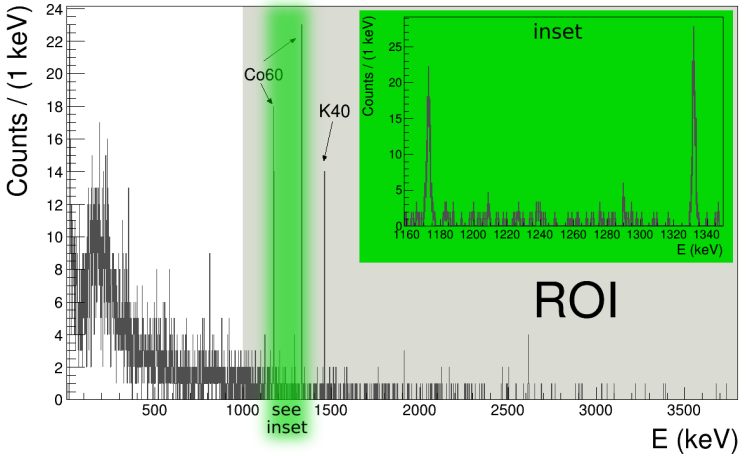

Figure 3: **Measured radiation spectrum.** The measured emission spectrum, corresponding to a data taking period of about 62 days, is represented as a dark grey histogram. The natural binning of 1 keV is used; the bin contents are shown without error bars, in order to appreciate the relative intensities of the residual radionuclides emission lines. The ^{60}Co and ^{40}K lines are also indicated. The inset zooms in the region of the ^{60}Co lines (which is highlighted in the total plot by the shadowed green area); here the error bars are shown and represent one standard deviation. The grey area shows the Region Of Interest (ROI) which is defined as $\Delta E = (1000 \div 3800)$ keV.

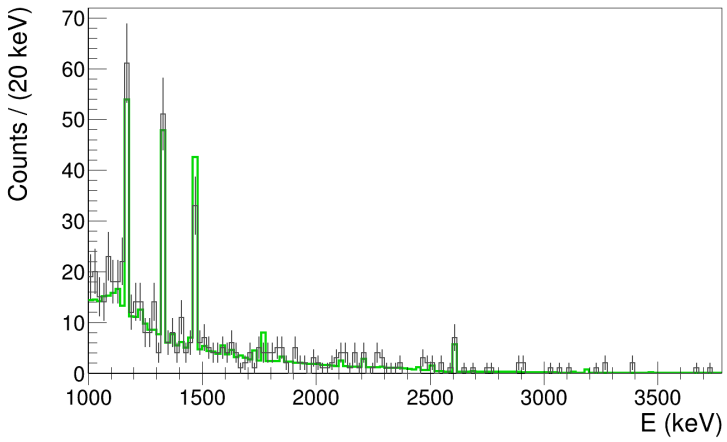

Figure 4: **Comparison between the measured and the simulated background spectra.** The measured emission spectrum is shown in the region of interest as a dark grey histogram, with error bars representing one standard deviation. The simulated background distribution is shown in green for comparison. The simulation is based on a GEANT 4 validated MC characterization of the whole detector. The MC has as input the measured activities of the residual radionuclides, for each material present in the experimental setup. The simulation accounts for the emission probabilities and the decay schemes, the photon propagation and interactions in the materials of the apparatus and the detection efficiencies (see Section Methods).

Then, we estimated the number of signal events which would be measured during the acquisition time, generated in the materials of the apparatus as collapse-induced photons. To this end the detection efficiencies were taken into account, which are shown, for the setup components which give an appreciable contribution, in Fig. 1 of the Supplementary Information.

Given the rate in Eq. (4) the expected signal contribution $z_s(R_0)$, which is a function of the

parameter R_0, turns out to be:

$$z_s(R_0) = \sum_i \int_{\Delta E} \left. \frac{d\Gamma_t}{dE} \right|_i T\epsilon_i(E)dE = \frac{a}{R_0^3}, \tag{5}$$

where T is the total acquisition time of the experiment, $\epsilon_i(E)$ is the energy dependent efficiency function for the i-th component of the setup and $a \sim 1.8 \times 10^{-29}$ m^3. By substituting the values z_c, z_b and z_s in the pdf of the parameter R_0 the following constraint is obtained:

$$R_0 > 0.54 \times 10^{-10}\,\text{m} \tag{6}$$

with probability 0.95. The data analysis is extensively described in the Supplementary Information, where the *pdf* is explicitly derived.

It is important to stress that the energy range in which spontaneous photon emission is expected, extends from the upper threshold of the detector sensitive region (3.8 MeV) to 100 MeV (according to the emission rate given in Eq. (4)). A fraction of these *primary* photons could be degraded in energy due to Compton scattering, thus producing additional events in the ROI. Such a process would result in a stronger lower bound on R_0. We made an estimate of the improvement (I) on the bound by considering the limiting case in which *all* the primary spontaneously emitted photons generated in the i-th component of the setup, in the energy range $(3.8 \div 100)$ MeV, are degraded, due to scattering, to the energy $E_i^{max,\,eff}$ within the ROI, corresponding to the maximal detection efficiency for the i-th material. We obtain $I \sim 1.620$, which is not sizeable (even under the exaggerated assumptions we considered); this is mainly due to the fact that spontaneous emission decreases with energy as $1/E$.

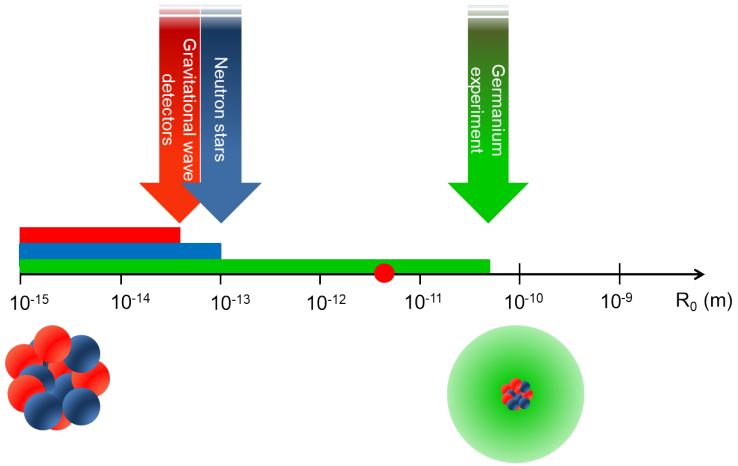

Figure 5: **Lower bounds on the spatial cut-off R_0 of the Diósi-Penrose (DP) model.** According to Penrose, the value of R_0 is estimated to be the size of the wave function of the nuclei of the system, which amounts to $R_0 = 0.05 \times 10^{-10}$ m for the Ge crystal used in the experiment (red bullet on the horizontal scale). Our experiment sets a lower bound on R_0 at 0.54×10^{-10} m (green bar and arrow), which is one order of magnitude larger than what predicted following Penrose's argument. Therefore, this parameter-free version of the DP model is excluded. The figure shows also previous lower bounds in the literature, similarly based on the monitoring of the Brownian-like diffusion predicted by the DP model. They refer to data analysis from gravitational wave detectors [36] ($R_0 \geq (40.1 \pm 0.5) \times 10^{-15}$ m, red bar and arrow) and neutron stars [42] ($R_0 \gtrsim 10^{-13}$ m, blue bar and arrow).

Our experiment sets a lower bound on R_0 of the order of $1\mathring{A}$, which is about three orders of magnitude stronger than previous bounds in the literature [36]; see Fig. 5. If R_0 is the size of the nucleus's wave function as suggested by Penrose, we have to confront our result with known properties of nuclei in matter. In a crystal, $R_0 = \sqrt{\langle u^2 \rangle}$ where $\langle u^2 \rangle$ is the mean square displacement

of a nucleus in the lattice, which can be computed by using the relation [43,44] $\langle u^2 \rangle = B/8\pi^2$, where $B = 0.20$ Å^2 is the Debye-Waller factor for the Germanium crystal [45], cooled down at the liquid Nitrogen temperature. One obtains $R_0 = 0.05 \times 10^{-10}$ m, which is more than one order of magnitude smaller than the lower limit set by our experiment. Therefore, we conclude that Penrose's proposal for a gravity-related collapse of the wave function, in the present formulation, is ruled out.

Of course, alternatives are always possible. Following Diósi, one option is to let R_0 completely free; but this comes at the price of having a parameter whose value is unjustified, apparently disconnected from the mass density of the system as well as from gravitational effects. Another option is to change the way the collapse is modeled (Poissonian decay), therefore adding extra terms and parameters to take into account a more complex dynamics, as done for other collapse models [46–48]. This kind of extensions was not envisaged in the literature so far. Our result indicates that the idea of gravity-related wave function collapse, which remains very appealing, will probably require a radically new approach.

1. Schrödinger, E. Die gegenwärtige Situation in der Quantenmechanik. *Naturwissenschaften* **23**, 823–828 (1935).

2. Leggett, A. J. Macroscopic quantum systems and the quantum theory of measurement. *Prog. Theor. Phys. Suppl.* **69**, 80–100 (1980).

3. Weinberg, S. Precision tests of quantum mechanics. *Phys. Rev. Lett.* **62**, 485–488 (1989).

4. Bell, J. S. *Speakable and unspeakable in quantum mechanics: Collected papers on quantum philosophy* (Cambridge university press, 2004).

5. Ghirardi, G. C., Rimini, A. & Weber, T. Unified dynamics for microscopic and macroscopic systems. *Phys. Rev. D* **34**, 470–491 (1986).

6. Adler, S. L. *Quantum theory as an emergent phenomenon: The statistical mechanics of matrix models as the precursor of quantum field theory* (Cambridge University Press, 2004).

7. Weinberg, S. Collapse of the state vector. *Phys. Rev. A* **85**, 062116 (2012).

8. Ghirardi, G. C., Pearle, P. & Rimini, A. Markov processes in Hilbert space and continuous spontaneous localization of systems of identical particles. *Phys. Rev. A* **42**, 78–89 (1990).

9. Bassi, A. & Ghirardi, G. Dynamical reduction models. *Phys. Rep.* **379**, 257–426 (2003).

10. Bassi, A., Lochan, K., Satin, S., Singh, T. P. & Ulbricht, H. Models of wave-function collapse, underlying theories, and experimental tests. *Rev. Mod. Phys.* **85**, 471–527 (2013).

11. Arndt, M. & Hornberger, K. Testing the limits of quantum mechanical superpositions. *Nat. Phys.* **10**, 271–277 (2014).

12. Feynman, R. *Feynman lectures on gravitation* (CRC Press, 2018).

13. Penrose, R. & Mermin, N. D. *The emperor's new mind: Concerning computers, minds, and the laws of physics* (Oxford University Press, Oxford, 1990).

14. Penrose, R. On gravity's role in quantum state reduction. *Gen. Rel. Gravit.* **28**, 581–600 (1996).

15. Penrose, R. On the gravitization of quantum mechanics 1: Quantum state reduction. *Found. Phys.* **44**, 557–575 (2014).

16. Howl, R., Penrose, R. & Fuentes, I. Exploring the unification of quantum theory and general relativity with a bose–einstein condensate. *New J. Phys.* **21**, 043047 (2019).

17. Diósi, L. A universal master equation for the gravitational violation of quantum mechanics. *Phys. Lett. A* **120**, 377–381 (1987).

18. Diósi, L. Models for universal reduction of macroscopic quantum fluctuations. *Phys. Rev. A* **40**, 1165–1174 (1989).

19. Ghirardi, G., Grassi, R. & Rimini, A. Continuous-spontaneous-reduction model involving gravity. *Phys. Rev. A* **42**, 1057–1064 (1990).

20. Diósi, L. Gravity-related wave function collapse: mass density resolution. *J. Phys. Conf. Ser.*, **442**, 012001 (2013).

21. Diósi, L. Gravitation and quantum-mechanical localization of macro-objects. *Phys. Lett. A* **105**, 199 – 202 (1984).

22. Bahrami, M., Großardt, A., Donadi, S. & Bassi, A. The Schrödinger–Newton equation and its foundations. *New J. Phys.* **16**, 115007 (2014).

23. Salart, D., Baas, A., van Houwelingen, J. A., Gisin, N. & Zbinden, H. Spacelike separation in a bell test assuming gravitationally induced collapses. *Phys. Rev. Lett.* **100**, 220404 (2008).

24. Marshall, W., Simon, C., Penrose, R. & Bouwmeester, D. Towards quantum superpositions of a mirror. *Phys. Rev. Lett.* **91**, 130401 (2003).

25. Kovachy, T. *et al.* Quantum superposition at the half-metre scale. *Nature* **528**, 530–533 (2015).

26. Fein, Y. Y. *et al.* Quantum superposition of molecules beyond 25 kDa. *Nature Physics* **15**, 1242–1245 (2019).

27. Lee, K. C. *et al.* Entangling macroscopic diamonds at room temperature. *Science* **334**, 1253–1256 (2011).

28. Chan, J. *et al.* Laser cooling of a nanomechanical oscillator into its quantum ground state. *Nature* **478**, 89–92 (2011).

29. Teufel, J. *et al.* Sideband cooling of micromechanical motion to the quantum ground state. *Nature* **475**, 359–363 (2011).

30. Wollman, E. E. *et al.* Quantum squeezing of motion in a mechanical resonator. *Science* **349**, 952–955 (2015).

31. Jain, V. *et al.* Direct measurement of photon recoil from a levitated nanoparticle. *Phys. Rev. Lett.* **116**, 243601 (2016).

32. Hong, S. *et al.* Hanbury brown and twiss interferometry of single phonons from an optomechanical resonator. *Science* **358**, 203–206 (2017).

33. Vovrosh, J. *et al.* Parametric feedback cooling of levitated optomechanics in a parabolic mirror trap. *J. Opt. Soc. Am. B* **34**, 1421–1428 (2017).

34. Riedinger, R. *et al.* Remote quantum entanglement between two micromechanical oscillators. *Nature* **556**, 473–477 (2018).

35. Bahrami, M., Smirne, A. & Bassi, A. Role of gravity in the collapse of a wave function: A probe into the Diósi-Penrose model. *Phys. Rev. A* **90**, 062105 (2014).

36. Helou, B., Slagmolen, B., McClelland, D. E. & Chen, Y. Lisa pathfinder appreciably constrains collapse models. *Phys. Rev. D* **95**, 084054 (2017).

37. Diósi, L. & Lukács, B. Calculation of X-ray signals from Károlyházy hazy space-time. *Phys. Lett. A* **181**, 366–368 (1993).

38. Neder, H., Heusser, G. & Laubenstein, M. Low level γ-ray germanium-spectrometer to measure very low primordial radionuclide concentrations. *Appl. Radiat. Isot.* **53**, 191–195 (2000).

39. Heusser, G., Laubenstein, M. & Neder, H. Low-level germanium gamma-ray spectrometry at the μbq/kg level and future developments towards higher sensitivity. *Radioactivity in the Environment* **8**, 495–510 (2006).

40. Fu, Q. Spontaneous radiation of free electrons in a nonrelativistic collapse model. *Phys. Rev. A* **56**, 1806–1811 (1997).

41. Piscicchia, K. *et al.* CSL collapse model mapped with the spontaneous radiation. *Entropy* **19**, 319 (2017).

42. Tilloy, A. & Stace, T. M. Neutron Star Heating Constraints on Wave-Function Collapse Models. *Phys. Rev. Lett.* **123**, 080402 (2019).

43. Debye, P. Interferenz von Röntgenstrahlen und Wärmebewegung. *Ann. d. Physik* **348**, 49–92 (1913).

44. Waller, I. Zur Frage der Einwirkung der Wärmebewegung auf die Interferenz von Röntgenstrahlen. *Zeitschrift für Physik* **17**, 398–408 (1923).

45. Gao, H. & Peng, L.-M. Parameterization of the temperature dependence of the Debye–Waller factors. *Acta Crystallogr., Sect. A: Found. Crystallogr.* **55**, 926–932 (1999).

46. Adler, S. L. & Bassi, A. Collapse models with non-white noises. *J. Phys. A* **40**, 15083 (2007).

47. Adler, S. L. & Bassi, A. Collapse models with non-white noises: II. Particle-density coupled noises. *J. Phys. A* **41**, 395308 (2008).

48. Gasbarri, G., Toroš, M., Donadi, S. & Bassi, A. Gravity induced wave function collapse. *Phys. Rev. D* **96**, 104013 (2017).

49. Breuer, H. P. & Petruccione, F. *The Theory of Open Quantum Systems* (Oxford University Press, Oxford, 2002).

50. Boswell, M. *et al.* Mage-a Geant4-based Monte Carlo application framework for low-background germanium experiments. *IEEE Trans. Nucl. Sci.* **58**, 1212–1220 (2011).

51. Adler S.L. & Ramazanoglu F.M., Photon-emission rate from atomic systems in the CSL model. *J. Phys. A* **40**, 13395 (2007). Corrigendum: Photon-emission rate from atomic systems in the CSL model. *J. Phys. A* **42**, 109801 (2009).

52. Adler S.L., Bassi A. & Donadi S., On spontaneous photon emission in collapse models. *J. Phys. A* **46**, 245304 (2013).

53. Bassi A. & Donadi S., Spontaneous photon emission from a non-relativistic free charged particle in collapse models: A case study. *Phys. Lett. A* **378**, 761–765 (2014).

54. Donadi S., Deckert D.-A., & Bassi A., On the spontaneous emission of electromagnetic radiation in the CSL model. *Ann. Phys. (N.Y.)* **340**, 70–86 (2014).

Acknowledgments

The authors thank Prof. S.L. Adler, Prof. M. Arndt and Prof. H. Ulbricht for useful discussions and comments, and C. Capoccia, Dr. M. Carlesso and Dr. R. Del Grande for their help in preparing the figures. S.D. acknowledges support from The Foundation BLANCEFLOR Boncompagni Ludovisi, née Bildt, INFN and the Fetzer Franklin Fund. K.P. and C.C. acknowledge the support of the Centro Fermi - Museo Storico della Fisica e Centro Studi e Ricerche "Enrico Fermi" (*Open Problems in Quantum Mechanics project*), the John Templeton Foundation (ID 58158) and FQXi. L.D. acknowledges support of National Research Development and Innovation Office of Hungary Nos. 2017-1.2.1-NKP-2017-00001 and K12435, and support by FQXI minigrant. A.B. acknowledges support from the H2020 FET TEQ (grant n. 766900), the University of Trieste and INFN. All authors acknowledge support from the COST Action QTSpace (n. CA15220).

Authors contributions

S.D. and A.B. conceived and designed the theoretical aspects of the research; M.L., K.P. and C.C. designed the experimental part of the research; S.D. performed the theoretical calculations, with the assistance of A.B. and L.D.; M.L., K.P. and C.C. performed the experimental measurements; K.P. performed the data analysis, with the assistance of C.C., M.L. and L.D.; S.D., K.P. and A.B. prepared the manuscript and Supplementary Information in coordination with all authors.

Competing interests

The authors declare no competing interests.

Supplementary Information is linked to the online version of the paper at www.nature.com/nature.

Methods

Calculation of the radiation emission rate. We summarize the main steps for deriving Eq. (4) for the emission rate of the main text. The starting point is the quantum mechanical formula for the radiation emission rate

$$\frac{d}{d\omega}\Gamma_t = \frac{k^2}{c}\sum_{\mu}\int d\Omega_k \frac{d}{dt}\langle a^{\dagger}_{\mathbf{k}\mu}a_{\mathbf{k}\mu}\rangle_t, \tag{7}$$

where $\langle a^{\dagger}_{\mathbf{k}\mu}a_{\mathbf{k}\mu}\rangle_t$ gives the average number of photons emitted at time t with wave vector $\boldsymbol{k}$ and polarization μ. The time derivative accounts for the fact that we are computing a rate; the integration

over the directions and polarizations of the photons for the fact that we are interested in the total number of photons emitted in a given energy range, independently from these degrees of freedom; and the factor $\frac{k^2}{c}$ for the density of wave vectors with modulus k.

The expectation value $\langle a^\dagger_{\mathbf{k}\mu} a_{\mathbf{k}\mu}\rangle_t$ is computed starting from the master equation (3) of the main text, which is convenient to rewrite in the following form [35]:

$$\frac{d\rho(t)}{dt} = -\frac{i}{\hbar}\left[H, \rho(t)\right] + \int d\boldsymbol{Q} \sum_{n,n'} \tilde{\Gamma}_{n,n'}(\boldsymbol{Q}) \left(e^{\frac{i}{\hbar}\boldsymbol{Q}\cdot\boldsymbol{x}_n} \rho(t) e^{-\frac{i}{\hbar}\boldsymbol{Q}\cdot\boldsymbol{x}_{n'}} - \frac{1}{2}\left\{ e^{-\frac{i}{\hbar}\boldsymbol{Q}\cdot\boldsymbol{x}_{n'}} e^{\frac{i}{\hbar}\boldsymbol{Q}\cdot\boldsymbol{x}_n}, \rho(t)\right\}\right) \tag{8}$$

where

$$\tilde{\Gamma}_{n,n'}(\boldsymbol{Q}) = \frac{4G}{\pi\hbar^2} \frac{\tilde{\mu}_n(\boldsymbol{Q})\tilde{\mu}^*_{n'}(\boldsymbol{Q})}{Q^2}. \tag{9}$$

with

$$\tilde{\mu}(\boldsymbol{Q}) = \frac{1}{2\pi\hbar^3} \int d\boldsymbol{y}\, \mu(\boldsymbol{y}) e^{-\frac{i}{\hbar}\boldsymbol{Q}\cdot\boldsymbol{y}} \tag{10}$$

the Fourier transform of the mass density $\mu(\boldsymbol{y})$.

We moved to the Heisenberg picture, introducing the adjoint master equation of Eq. (8), which for a generic operator O takes the form [49]:

$$\frac{d}{dt}O(t) = \frac{i}{\hbar}\left[H, O(t)\right] + \int d\boldsymbol{Q} \sum_{k,k'} \tilde{\Gamma}_{k,k'}(\boldsymbol{Q}) \left(e^{-\frac{i}{\hbar}\boldsymbol{Q}\cdot\boldsymbol{x}_{k'}} O(t) e^{\frac{i}{\hbar}\boldsymbol{Q}\cdot\boldsymbol{x}_k} - \frac{1}{2}\left\{ O(t), e^{-\frac{i}{\hbar}\boldsymbol{Q}\cdot\boldsymbol{x}_{k'}} e^{\frac{i}{\hbar}\boldsymbol{Q}\cdot\boldsymbol{x}_k}\right\}\right). \tag{11}$$

The total Hamiltonian H is the sum of three contributions:

$$H = H_{\text{S}} + H_{\text{R}} + H_{\text{INT}}. \tag{12}$$

The first term is:

$$H_{\text{S}} = \sum_j \left(\frac{\boldsymbol{p}_j^2}{2m_j} + V(\boldsymbol{x}_j) + \sum_{i<j} U(\boldsymbol{x}_j - \boldsymbol{x}_i) \right) \tag{13}$$

where the sums run over all particles of the system; V is an external potential and U the potential among the particles of the system. We specialize on the emission from a crystal, therefore the sum will run over all the electrons and the nuclei of the system (given the energy range of the emitted photons we consider, we do not need to resolve the internal structure of the nuclei by considering their protons). The free electromagnetic Hamiltonian is

$$H_{\text{R}} = \sum_\mu \int d\boldsymbol{k} \hbar\omega_k \left(\frac{1}{2} + a^\dagger_{\boldsymbol{k},\mu} a_{\boldsymbol{k},\mu} \right) \tag{14}$$

where $\omega_k = kc$ and $a_{\boldsymbol{k},\mu}$, $a^\dagger_{\boldsymbol{k},\mu}$ are, respectively, the annihilation and creation operators of a photon with wave-vector $\boldsymbol{k}$ and polarization μ. The last term describes the usual interaction between the electromagnetic field and the particles (at the non-relativistic level):

$$H_{\text{INT}} = \sum_j \left(-\frac{e_j}{m_j} \right) \boldsymbol{A}(\boldsymbol{x}_j) \cdot \boldsymbol{p}_j + \sum_j \frac{e_j^2}{2m_j} \boldsymbol{A}^2(\boldsymbol{x}_j), \tag{15}$$

where e_j, m_j are the charge and the mass of the j-th particle of the system and $\boldsymbol{A}(\boldsymbol{x})$ is the vector potential which can be expanded in plane waves as:

$$\boldsymbol{A}(\boldsymbol{x}) = \int d\boldsymbol{k} \sum_\mu \alpha_k \left[\vec{\epsilon}_{\boldsymbol{k},\mu}\, a_{\boldsymbol{k},\mu}\, e^{i\boldsymbol{k}\cdot\boldsymbol{x}} + \vec{\epsilon}_{\boldsymbol{k},\mu}\, a^\dagger_{\boldsymbol{k},\mu}\, e^{-i\boldsymbol{k}\cdot\boldsymbol{x}} \right] \tag{16}$$

with $\alpha_k = \sqrt{\frac{\hbar}{2\varepsilon_0 \omega_k (2\pi)^3}}$, ε_0 the vacuum permittivity and $\vec{\epsilon}_{\boldsymbol{k},\mu}$ the (real) polarization vectors. Note that in Eq. (15) the term proportional to $\boldsymbol{p}_j \cdot \boldsymbol{A}(\boldsymbol{x}_j)$ is missing because we are working in the Coulomb gauge where $\nabla \cdot \boldsymbol{A} = 0$, implying $\vec{\epsilon}_{\boldsymbol{k},\mu} \cdot \boldsymbol{k} = 0$; therefore this term contributes in the same way as the term $\boldsymbol{A}(\boldsymbol{x}_j) \cdot \boldsymbol{p}_j$ and the two can be added.

Starting from Eq. (11), the average number of photons emitted at time t $\langle a^\dagger_{\mathbf{k}\mu} a_{\mathbf{k}\mu}\rangle_t$ is computed and then inserted in Eq. (7) to find the rate. The calculation is long but conceptually simple: the integral form of Eq. (11) is expanded perturbatively up to the second order (the first order terms give no contribution), similarly to what is usually done when the evolution operator is expanded using the Dyson series. Then one has to compute the nine terms resulting from this expansion. The calculation is fully reported in the Supplementary Information; here we give the physical picture underlying the calculations, which proved to be successful when applied to other models of spontaneous wave function collapse [40,51–54].

One can understand the mechanism of radiation emission in terms of a semi-classical picture. Each time there is a collapse, particles are "kicked", corresponding to an acceleration with associated radiation emission. The radiation emitted from different particles may add coherently or incoherently and to understand under which conditions they occur, it is instructive to study the radiation emission from two charged particles in the context of classical electrodynamics.

Suppose the two particles are accelerated by the same external force. At a point "x" very far away from the charges, the values of the emitted radiation crucially depends both on the distance L between the particles and the wavelength λ of the emitted radiation. If the charges have opposite signs, when $L \ll \lambda$, given $x \gg L, \lambda$, the electric fields $E_1(x)$ generated by the positive charge and $E_2(x)$ generated by the negative charge will be the same, just with opposite sign, due to the opposite value of the charges. Then in this case $E_{\text{tot}}(x) = E_1(x) + E_2(x) \simeq 0$, and because the emitted radiation is proportional to $|E_{\text{tot}}(x)|^2$, there is almost a full cancellation of the radiation

field. On the contrary, if both charges have the same sign, $E_{\text{tot}}(x) = E_1(x) + E_2(x) \simeq 2E_1(x)$, hence the emitted radiation becomes four times larger than that emitted by a single charge. In more informal terms, we can say that for $L \ll \lambda$ a detector at x sees the charges as if they are sitting in the same point. This leads to a coherent emission which suppresses the radiation emitted when the particles have opposite charges and maximizes it when they have the same charge.

On the contrary, let us now consider the case $L \gg \lambda$. Still assuming $x \gg L, \lambda$, the two electric fields $E_1(x)$ and $E_2(x)$ have in general different intensities. In fact, if we label by $x_1(x_2)$ the distance between the point "x" and the point where the first (second) particle is located, we have $|x_1 - x_2| \sim L$. Then the electric fields oscillate many times in the distance $|x_1 - x_2|$. Therefore, even if at a given point "x" they perfectly cancel, in a nearby point "$x+dx$" they add constructively. As for the intensity, one has $I(x) \propto |E_{\text{tot}}(x)|^2 = |E_1(x)|^2 + |E_2(x)|^2 + E_1^*(x)E_2(x) + E_1(x)E_2^*(x)$, and when we integrate over a spherical surface of radius $|x|$, to find the total emission rate, the last two terms average to zero due to the fast oscillating behavior, and one gets that the two particles emit independently.

Going back to the calculation in the main text, since the distance between electrons and nuclei is of order of one Angstrom, while the wavelength of the photons we are considering in the experiment is much smaller ($3.3 \times 10^{-3} < \lambda < 1.2 \times 10^{-2}$ Angstrom), we are precisely in the second situations described here above, so electrons and nuclei emit independently. On the contrary, protons in the same nucleus are much closer than the smallest wavelength of the photons we are considering, which explains why they emit coherently. As a result, the emission rate from

the crystal is given by Eq. (4) of the main text, where the emission from the electrons is neglected and the incoherent emission from all atoms in the crystal is considered.

As a final note, in the DP model there is another reason for the incoherent radiation by electrons and nuclei, as long as $R_0 \ll L$ (which holds in our case). The gravitational fluctuations, underlying the decoherence term of Eq. (3), which accelerate the charges, become uncorrelated beyond the range R_0: the electrons and the nuclei are accelerated by uncorrelated "kicks", resulting in an induced incoherent emission.

Statistical analysis. Each component of the experimental apparatus was characterized by means of MC simulations (see [50]) based on the GEANT4 software library (verified by participating to international proficiency tests organised by the IAEA). The simulations were used to determine *i*) the expected background due to residual radionuclides in the materials of the setup, *ii*) the expected spontaneous radiation emission contribution to the measured spectrum. More in detail:

- *i*) the MC simulation of the background is based on the measured activities of the residual radionuclides, in all the components of the setup. The simulation accounts for the emission probabilities and the decay schemes, the photon propagation and interactions in the materials of the apparatus and the detection efficiencies. The obtained spectrum is compared with the measured distribution in Fig. 4.

- *ii*) the efficiency, as a function of the energy, for the detection of spontaneously emitted photons was obtained by generating 10^8 photons, for each component of the setup, in steps

of 200 keV (i.e. 15 points in the ROI $\Delta E = E_1 \div E_2 = (1000 \div 3800)$ keV). The efficiency functions $\epsilon_i(E)$, i labelling the material of the detector, were then estimated from polynomial fits of the corresponding distributions. Given the rate in Eq. (4) one expects to measure a number of events:

$$\int_{\Delta E} \left. \frac{d\Gamma_t}{dE} \right|_i T\epsilon_i(E)dE, \tag{17}$$

due to the spontaneous emission by protons belonging to the i-th material, during the acquisition time T. Summing over all the materials, the total signal contribution (see Eq. (5)) is obtained: $z_s(R_0) = a/R_0^3$.

The stochastic variable, representing the total number of photon counts measured in the range ΔE, follows a Poisson distribution:

$$p(z_c|\Lambda_c) = \frac{\Lambda_c^{z_c} e^{-\Lambda_c}}{z_c!}, \tag{18}$$

with Λ_c the corresponding expected value. Two sources contribute to the measured spectrum: a background (b) originated by all known emission processes, together with a potential signal (s) due to spontaneously emitted photons induced by the collapse process. The total number of counts, respectively z_b and z_s, which would be measured in the period T, were estimated according to i and ii. The corresponding independent stochastic variables can be also associated to Poisson distributions, whose expected values (Λ_b and Λ_s) are then related by:

$$\Lambda_c(R_0) = \Lambda_b + \Lambda_s(R_0) = z_b + z_s(R_0) + 2 \tag{19}$$

where the dependence on R_0 is explicitly shown.

The pdf of $\Lambda_c(R_0)$ can then be obtained from Eq. (18) by applying the Bayes theorem:

$$\tilde{p}\left(\Lambda_c(R_0)|p(z_c|\Lambda_c(R_0))\right) = \frac{p(z_c|\Lambda_c(R_0)) \cdot \tilde{p}_0(\Lambda_c(R_0))}{\int_D p(z_c|\Lambda_c(R_0)) \cdot \tilde{p}_0(\Lambda_c(R_0))\, d[\Lambda_c(R_0)]}, \tag{20}$$

with D the domain of Λ_c and $\tilde{p}_0$ the prior distribution. R_0 is constrained by the requirement $R_0 > R_0^{min} = 10^{-14}$ m, which implies an upper bound on Λ_c (see Eq. (19)). We then used a Heaviside function for the prior

$$\tilde{p}_0(\Lambda_c(R_0)) = \theta(\Lambda_c^{max} - \Lambda_c(R_0)), \tag{21}$$

with $\Lambda_c^{max} = \Lambda_c(R_0^{min})$. From Eq. (20) the pdf of $\Lambda_c(R_0)$ is:

$$\tilde{p}\left(\Lambda_c(R_0)\right) = \frac{\Lambda_c^{z_c}\, e^{-\Lambda_c}\, \theta(\Lambda_c^{max} - \Lambda_c)}{\int_0^{\Lambda_c^{max}} \Lambda_c^{z_c}\, e^{-\Lambda_c}\, d\Lambda_c}. \tag{22}$$

In order to obtain the bound given in Eq. (6) one then has to solve the following integral equation for the cumulative pdf:

$$\tilde{P}\left(\bar{\Lambda}_c\right) = \frac{\gamma(z_c + 1, \bar{\Lambda}_c)}{\gamma(z_c + 1, \Lambda_c^{max})} = 0.95 \tag{23}$$

which yields $\Lambda_c < \bar{\Lambda}_c = 617$. As a consequence

$$\Lambda_c(R_0) = \Lambda_s(R_0) + \Lambda_b < 617 \Rightarrow \frac{a}{R_0^3} + \Lambda_b + 1 < 617 \Rightarrow R_0 > \sqrt[3]{\frac{a}{616 - \Lambda_b}}. \tag{24}$$

The analysis was performed in the energy range $E_1 \div E_2$ in which all the hypotheses of the model, for the spontaneous emission of protons, are fulfilled. However the energy range in which spontaneous photon emission is expected, according to Eq. (4), extends up to 100 MeV. A fraction of spontaneously emitted photons with energy $E \in E_2 \div E_3 = (3.8 \div 100)$ MeV could be degraded in energy due to Compton scattering, thus contributing to $\Lambda_s(R_0)$; for this reason we estimated the

corresponding improvement (I) to the bound in Eq. (6). Any improvement in the description of the expected background (or signal) contribution would lead to a bigger value of Λ_b (or a), and from Eq. (24) one can infer that this would translate in a stronger bound on R_0.

Regarding Λ_b, since the MC simulation is based on the measured activities, we do not expect a contribution to photon emission, at energies higher than 3.8 MeV, originated from radionuclides decays.

The total number of spontaneously emitted photons which are generated in the materials of the detector in the energy range $E_2 \div E_3$ is given by:

$$\sum_i \int_{E_2}^{E_3} \left.\frac{d\Gamma_t}{dE}\right|_i T\, dE = \sum_i \int_{E_2}^{E_3} N_i^2\, N_{ai}\, \beta\, T\, \frac{1}{R_0^3 E} dE = \frac{b}{R_0^3} > 0, \tag{25}$$

where N_i and N_{ai} are, respectively, the number of protons contained in each atom and the number of atoms of the i-th material, while the constant β is defined as:

$$\beta = \frac{2}{3} \frac{G e^2}{\pi^{3/2} \varepsilon_0 c^3}, \tag{26}$$

G, e, ε_0 and c are constants of nature with the usual meaning. Let us indicate with f the fraction of these photons which, due to Compton scattering, produce events in the ROI and are detected. The total signal contribution turns then to be:

$$z_s(R_0) = \frac{a}{R_0^3} + \frac{f\, b}{R_0^3} > \frac{a}{R_0^3}. \tag{27}$$

Since $a + f\, b > a$, the contribution of the spontaneous emission in the range $E_2 \div E_3$ improves the bound on R_0 by a factor $\sqrt[3]{(a + f\, b)/a}$.

We extracted the maximal improvement I under the extreme - nontheless most conservative - assumption that *all* the primary spontaneously emitted photons generated in the i-th material, in the energy range $E_2 \div E_3$, are degraded, due to scattering, to the energy $E_i^{max,\,eff} \in E_1 \div E_2$ which corresponds to the maximal efficiency for the corresponding material (see Fig. 1 of the Supplementary Information). The total signal contribution then amounts to:

$$\begin{aligned} z_s(R_0) = & \sum_i \int_{E_1}^{E_2} \left.\frac{d\Gamma}{dE}\right|_i T\,\epsilon_i(E)\,dE + \sum_i \epsilon_i^{max} \int_{E_2}^{E_3} \left.\frac{d\Gamma}{dE}\right|_i T\,dE = \\ & = \left((1.756 + 5.712)\,\times 10^{-29}\right)\,\frac{\mathrm{m}^3}{R_0^3} = \frac{a + f\,b}{R_0^3} \end{aligned} \tag{28}$$

which corresponds to an improvement $I \sim 1.620$. The improvement is not sizeable, as stated in the main text, even under the exaggerated assumptions we considered.

Data availability

Source data are available for this paper. All other data that support the plots within this paper and other findings of this study are available from the corresponding author upon reasonable request.

Code availability

The MC simulation is based on the GEANT4 code which is freely accessible. Experimental details inside are protected by non-disclosure agreement.